



OPEN ACCESS

EDITED BY

Juan Carlos Jauregui,
Autonomous University of Queretaro, Mexico

REVIEWED BY

Joshuva Arockia Dhanraj,
Dayananda Sagar University, India
Yunhui Huang,
Wuhan University of Technology, China
Li Sun,
Harbin Institute of Technology, Shenzhen,
China

*CORRESPONDENCE

Wanning Zheng,
✉ zhengwanning@uwust.edu.cn

RECEIVED 30 January 2024

ACCEPTED 30 May 2024

PUBLISHED 16 July 2024

CITATION

Jiang K, Ye C, Zheng W, Chen Y, Xiong P, Li L
and Hu P (2024), Relative stability evaluation
of HVDC-connected wind farms.
Front. Energy Res. 12:1379009.
doi: 10.3389/fenrg.2024.1379009

COPYRIGHT

© 2024 Jiang, Ye, Zheng, Chen, Xiong, Li and
Hu. This is an open-access article distributed
under the terms of the [Creative Commons
Attribution License \(CC BY\)](#). The use,
distribution or reproduction in other forums is
permitted, provided the original author(s) and
the copyright owner(s) are credited and that
the original publication in this journal is cited,
in accordance with accepted academic
practice. No use, distribution or reproduction
is permitted which does not comply with
these terms.

Relative stability evaluation of HVDC-connected wind farms

Kezheng Jiang¹, Chang Ye¹, Wanning Zheng^{2*}, Yang Chen²,
Ping Xiong¹, Lie Li¹ and Pan Hu¹

¹State Grid Hubei Electric Power Research Institute, Wuhan, China, ²Department of Information Science and Engineering, Wuhan University of Science and Technology, Wuhan, China

The small-signal stability of high voltage direct current (HVDC)-connected wind farms (WFs) is a challenging issue in modern power systems. The relative stability, i.e., the stability margin, of such a typical multiple-input multiple-output (MIMO) system is quite difficult to be quantified. This paper evaluates the relative stability of HVDC-connected WFs using a new stability index based on the ν -gap metric. We first develop a MIMO model represented by a transfer function matrix of the HVDC-connected WFs. Then, a new stability index, i.e., the robust stability margin, based on the ν -gap metric is proposed to quantify the relative stability of such a MIMO system. Finally, we propose a method to compute the stable region of control parameters based on the corresponding stability criterion of ν -gap metric. Case studies are given to demonstrate the effectiveness of the proposed method.

KEYWORDS

wind farms, HVDC, ν -gap metric, robust stability margin, stable region

1 Introduction

Nowadays, line-commutated converter based HVDC system is widely used for long-distance transmission of renewable energies, especially in China. In recent years, several subsynchronous oscillations have occurred in the HVDC systems connected with renewable energy generations, e.g., the oscillation phenomena in the Hami grid of China's Xinjiang Province, which seriously threaten the stability of modern power systems.

The small-signal stability of HVDC-connected WFs has attracted a lot of attention from researchers. Eigenvalue analysis method is one of the commonly used approach for stability analysis (Zhou et al., 2011; Yogarathinam et al., 2017; Ángel Cardiel-Álvarez et al., 2017). Based on the state-space model of the overall system, the eigenvalues, participation factors and sensitivity of control parameters are calculated (Yogarathinam et al., 2017; Ángel Cardiel-Álvarez et al., 2017; Shen et al., 2021). Some insights of the oscillations can be found from the analysis results. A state-space model of Gravelines generator and IFA2000 HVDC system is established (Kovacevic et al., 2019). The results show that damping of the 6.3 Hz mode can be improved while the damping of 12 Hz mode can be deteriorated by increasing the proportional parameters of DC current controller and PLL.

Impedance analysis is also a widely used method to analyze the stability of the HVDC-connected WFs. The impedance models of HVDC-connected WFs are developed in (Liu and Sun, 2013a; b), and the stability of the systems are analyzed based on the Nyquist criterion (Sun, 2011; Liu et al., 2014; Wang et al., 2022b). Researchers compared the influence of different control parameters on the impedance characteristics of the system in (Wang et al., 2022a; Wang et al., 2020). Considering the effect of DC control system, an impedance modeling method of control system based on transfer function is proposed

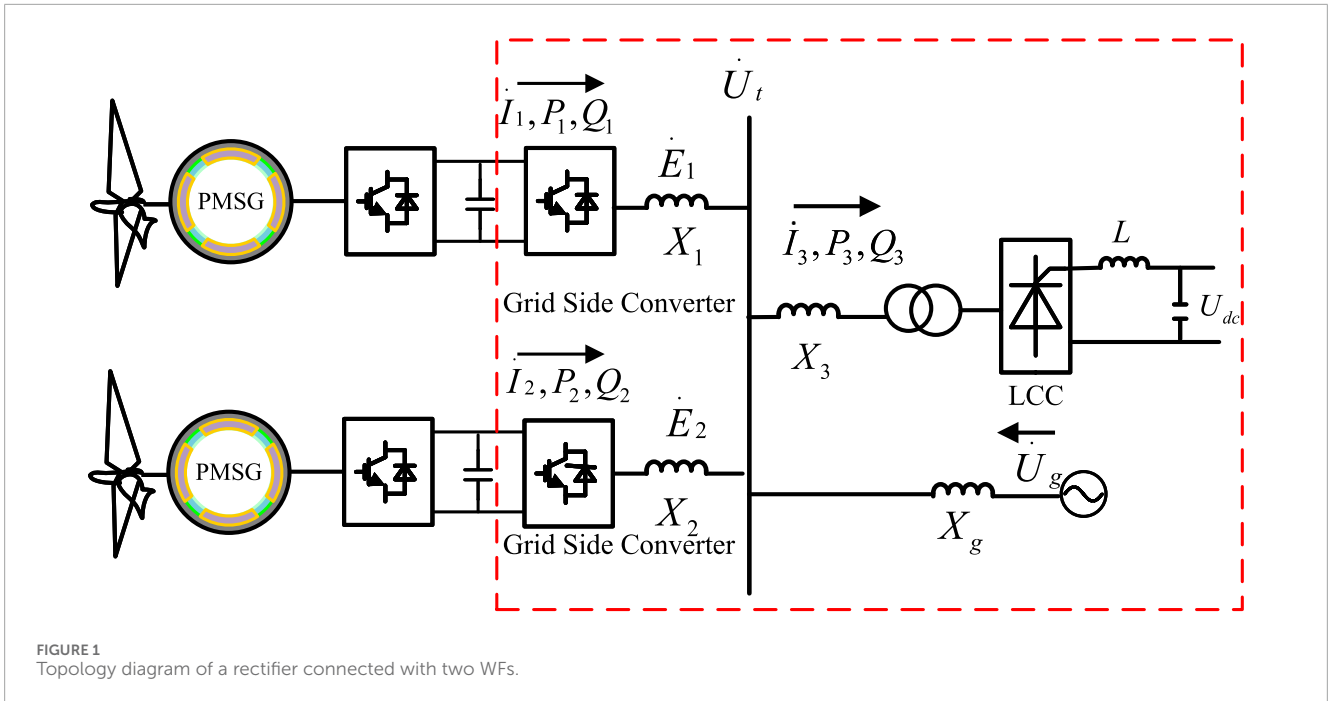


FIGURE 1
Topology diagram of a rectifier connected with two WFs.

in (Su et al., 2023). The results show that the constant current control of the rectifier has resonance risk near a specific frequency.

However, the above methods mainly focus on determining whether the system is stable or not. It is difficult for them to assess the relative stability, i.e., the stability margin, of the system and measure how far the system is away from instability. A better relative stability performance indicates that the system can tolerate a larger range of parameter variation.

On the other hand, gain margin and phase margin are measurements of the relative stability of a single-input single-output (SISO) system in classical control theories. Researchers use gain and phase margin to analyze and design the control systems in the context of robust stabilization (Bayhan and Soylemez, 2007). Based on the impedance model of WFs, phase and gain margin can be calculated from Nyquist curve (Rohit et al., 2021). However, since phase and gain margin are calculated by the open-loop transfer function of a unit feedback system, they are only available for SISO systems. It is difficult to compute the phase and gain margin of the HVDC-connected WFs, which is a typical MIMO system with multiple devices. To address this issue, we come up with the idea of applying the *v-gap metric* to measure the stability margin of the system. The *v-gap metric theory* is commonly used to investigate the robustness of stability in feedback interconnected systems (Vinnicombe, 2001; Jiang et al., 2021), especially for MIMO systems.

In this paper, we analyze the relative stability of a HVDC system connected with WFs utilizing the *v-gap metric*. The contributions of this paper are as follows: 1) We build a small-signal model of a HVDC system connected with WFs represented by transfer function matrix, in which the internal current vector and the active/reactive power are the input and output signals. 2) A new stability index, i.e., the robust stability margin, based on the *v-gap metric* is proposed to quantify the relative stability of such a MIMO system. Compared with phase and gain margin, the proposed robust stability margin can be calculated directly on the basis of the proposed MIMO model

of the system. 3) Based on the sufficient and necessary stability criterion of the *v-gap metric*, we propose a method to compute the stable region of the control and operation parameters of the system.

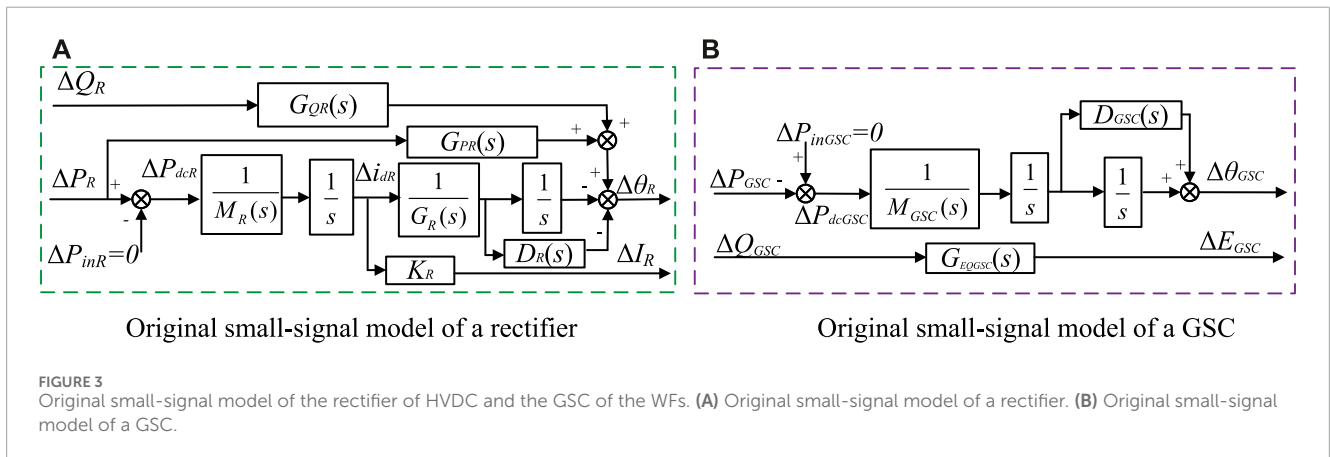
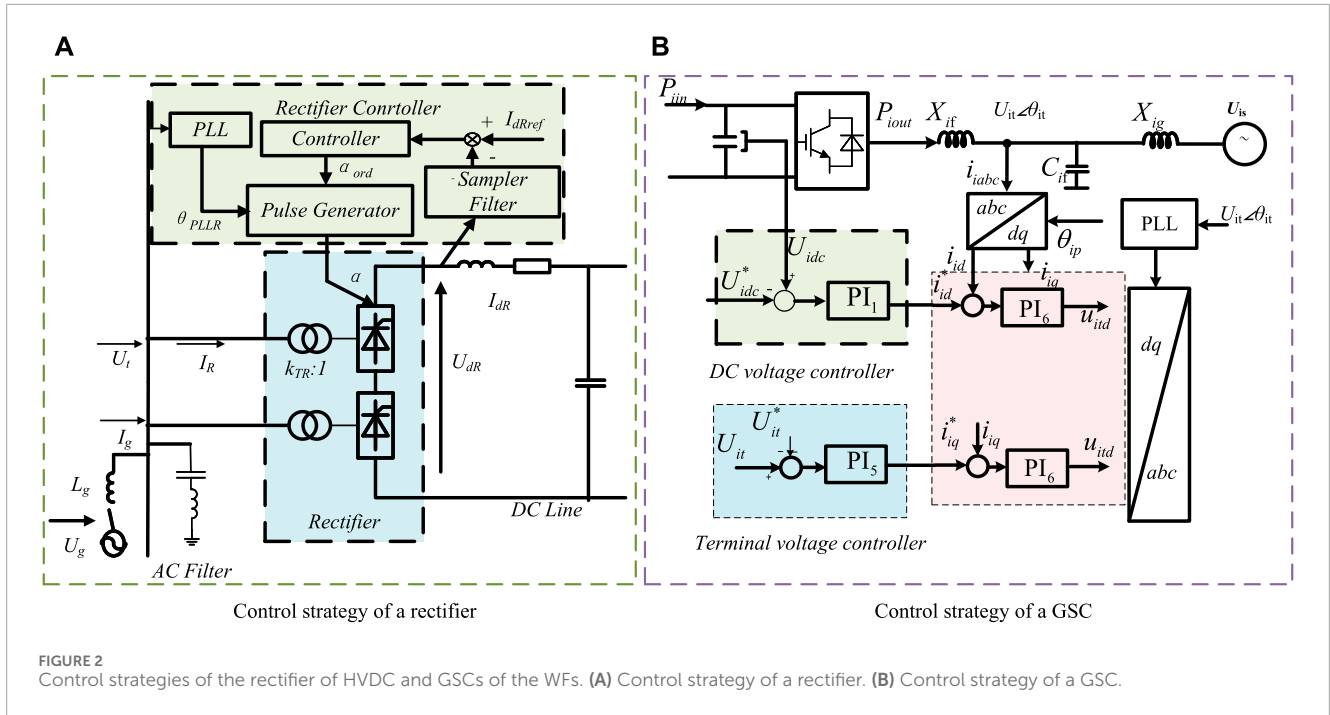
The rest of this paper is organized as follows. Chapter 2 presents the original small-signal model of HVDC-connected WFs and the basic definitions of the *v-gap metric*. Chapter 3 develops a standardized feedback model of HVDC-connected WFs applicable to the *v-gap metric*. Furthermore, the robust stability margin and the method to compute the stable region of control and operation parameters is presented in Chapter 4. Simulation results are proposed in Chapter 5, and conclusions are drawn in Chapter 6.

2 Related work

In this section, we show the related work of this paper. Firstly, we present the original small-signal model proposed in (Yuan et al., 2017; Lu et al., 2020) based on the typical control scheme of a HVDC system and WFs. Then, the basic definitions and the stability criterion based on the *v-gap metric* are introduced.

2.1 Original small-signal model in DVC timescale

Figure 1 shows a HVDC system connected with two WFs. This paper mainly focuses on the power sending terminal containing the rectifier of the HVDC and the GSCs of the WFs. In such a system, P and Q represent active power and reactive power. \dot{E} and \dot{I} represent the voltage and current vectors of each equipment. \dot{U}_t represents the voltage vector at the point of common coupling. X represents the reactance between each equipment and the grid connection point. Subscripts 1, 2, 3, g represent GSC 1, GSC 2, a rectifier, and infinite bus, respectively.



According to (Lu et al., 2020), Figure 2A shows the typical control strategy of the rectifier of a HVDC system. DC current control (DCC) is applied to control the DC current and generate an appropriate order triggering angle α_{ord} for the thyristors. At the same time, a phase-locked loop (PLL) is used to capture the phase of the AC terminal voltage. The value of α_{ord} is the sum of actual triggering angle and PLL's angle.

Figure 2B depicts the typical control strategy of a GSC, including DC voltage control (DVC), reactive power control (RPC), inner current control (ICC) and PLL. The active branch controls the DC voltage and the AC current in d-axis. The reactive branch controls the reactive power and the AC current in q-axis. Similar with the rectifier of HVDC, all the above control are controlled on the PLL synchronization reference frame.

Utilizing the above control strategies, the small-signal models of a rectifier and a GSC in DVC timescale (about 10 Hz) are proposed in (Yuan et al., 2017; Lu et al., 2020), respectively. Figure 3A depicts the original small-signal model of a rectifier. Figure 3B depicts the

original small-signal model of a GSC. In these models, the active and reactive power are the input signals and the phase and magnitude of the internal voltage or current are the output signals. They describe the dynamic characteristics of the rectifier and the GSC with clear mechanism understanding based on the motion equation concept.

2.2 Basic theory of ν -gap metric

The basic theory of ν -gap metric is proposed (Zhou, 2010) to analyze the robust stability of a feedback system. Consider a nominal feedback system depicted in Figure 4A. $P(s)$ is the forward channel and $C(s)$ is the feedback channel. The robust stability margin to quantify the relative stability is denoted as $b[P(s), C(s)]$. If the system is stable, $b[P(s), C(s)]$ is in the interval (0,1]. If the system is unstable, $b[P(s), C(s)] = 0$.

For the corresponding feedback system with uncertainties as shown Figure 4B. $\tilde{P}(s)$ and $\tilde{C}(s)$ are sets of uncertainties around the

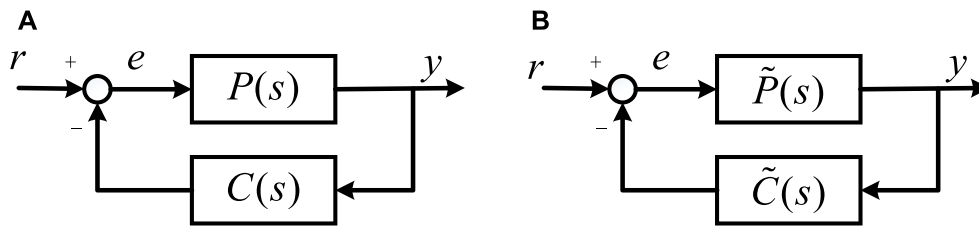


FIGURE 4 Standard model block diagram. The left image is (A), and the right image is (B).

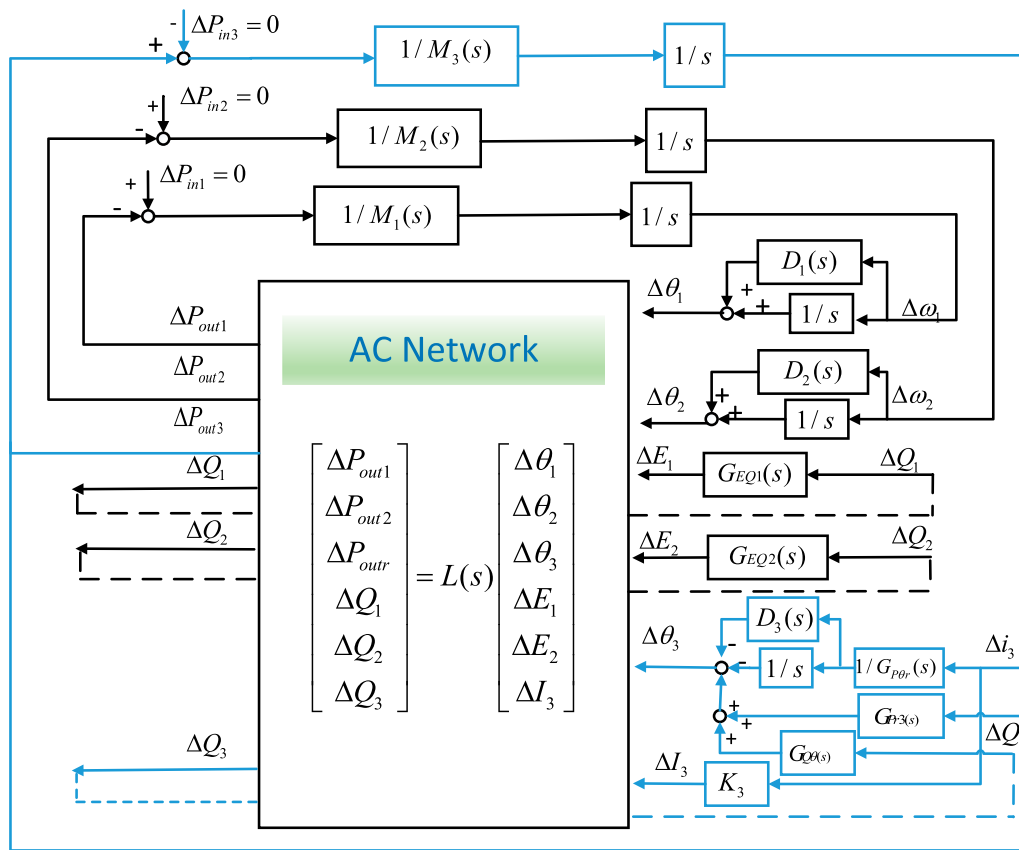


FIGURE 5 Small signal model.

given system $P(s)$ and $C(s)$. Denote the distance between $P(s)$ and $\tilde{P}(s)$ as $v[P(s), \tilde{P}(s)]$. Denote the distance between $C(s)$ and $\tilde{C}(s)$ as $v[C(s), \tilde{C}(s)]$. If

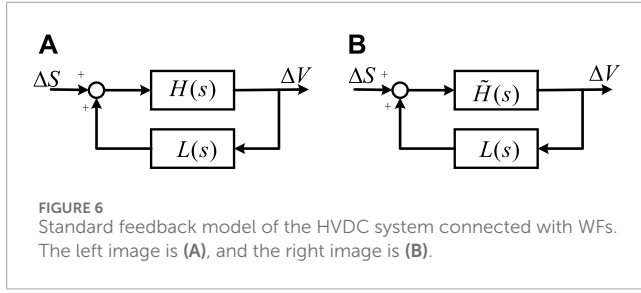
$$v[P(s), \tilde{P}(s)] + v[C(s), \tilde{C}(s)] < b[P(s), C(s)] \quad (1)$$

the uncertain system is stable. Otherwise, the uncertain system is unstable.

It is worth noticing that the system can be a SISO system or a MIMO system. Furthermore, the stability criterion is a necessary and sufficient condition without any conservatism.

3 Modeling of a HVDC system connected with WFs

In this section, based on the original small-signal model in Figure 5, we build a MIMO system model for the relative stability analysis. First, we present the forward channel of the MIMO system model by transfer function matrix. Then, we establish the feedback channel reflecting the power flow in AC network by transfer function matrix.



3.1 Modeling of the forward channel

In this subsection, we build the forward channel of the MIMO system model reflecting the dynamic characteristics of the rectifier and GSCs.

On the basis of the rectifier model shown in Figure 3A the GSC model shown in Figure 3B, we establish the small-signal model of the HVDC system connected with two GSCs in Figure 5. In this model, ΔP_{in} represents the active power input of the DC inductance and DC capacitors of each device. ΔP_{out} and ΔQ_{out} represent the active and reactive power output of the DC inductance and DC capacitors of each device. $\Delta\theta$ and ΔE represent the phase and magnitude of the internal voltage. Denote $\Delta\theta$ and ΔI as phase and magnitude of the internal current of the rectifier. Transfer functions $M(s)$ and $D(s)$ represent the equivalent inertia and damping, respectively. $G_{EQ}(s)$ is the transfer function related to the reactive power control. $G_{Pr3}(s)$ is a partial transfer function between ΔP_{out} and $\Delta\theta$ of the rectifier. Denote Δi_3 as AC current of the rectifier. $G_{p\theta r}(s)$ is a partial transfer function between Δi_3 and $\Delta\theta$ of the rectifier. K_3 is a proportionality transfer function between DC current dynamics and ΔI of the rectifier. $J_{6 \times 6}$ is an admittance matrix of the power flow in AC network. Specific expressions of the matrix and the transfer functions are provided in Supplementary Appendix SA according to (Yuan et al., 2017; Lu et al., 2020).

For the GSCs in the model, the transfer function between $\Delta\theta$ of the internal voltage and ΔP_{out} of GSC 1 can be expressed as

$$G_{p\theta 1}(s) = \frac{sD_1(s) + 1}{s^2M_1(s)}. \quad (2)$$

The transfer function between $\Delta\theta$ of the internal voltage and ΔP_{out} of GSC 2 can be described as

$$G_{p\theta 2}(s) = \frac{sD_2(s) + 1}{s^2M_2(s)}. \quad (3)$$

For the rectifier in the model, denote the transfer function $G_{p\theta 3}(s)$ between $\Delta\theta$ of the internal current and ΔP_{out} of the rectifier as

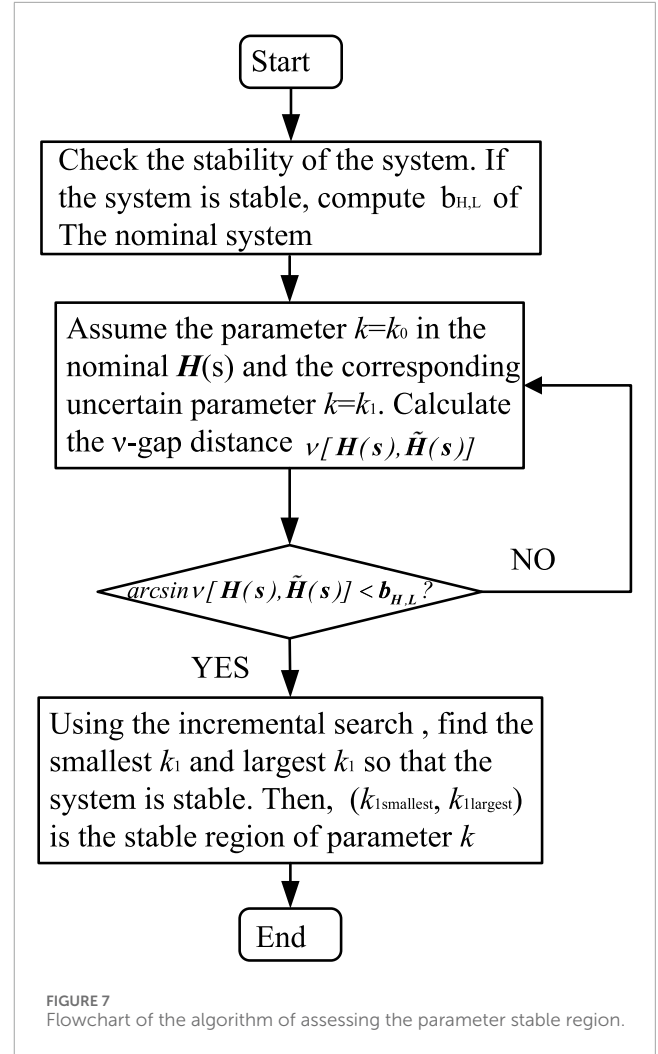
$$G_{p\theta 3}(s) = -\frac{sD_3(s) + 1}{s^2M_3(s)G_{p\theta r}(s)} + G_{Pr3}(s). \quad (4)$$

The transfer function between ΔI and ΔP_{out} of the rectifier can be described as

$$G_{PI3}(s) = \frac{K_3}{sM_3(s)}. \quad (5)$$

Specific expressions of G_{EQ1} , G_{EQ2} , $G_{Q\theta}$ are given in (Lu et al., 2020). For compact expressions, denote

$$\begin{aligned} \Delta V &= [\Delta\theta_1 \quad \Delta\theta_2 \quad \Delta\theta_3 \quad \Delta E_1 \quad \Delta E_2 \quad \Delta I_3]^T, \\ \Delta S &= [\Delta P_{out1} \quad \Delta P_{out2} \quad \Delta P_{out3} \quad \Delta Q_1 \quad \Delta Q_2 \quad \Delta Q_3]^T. \end{aligned} \quad (6)$$



Then, the forward channel of the MIMO system can be described as

$$\Delta V = H(s)\Delta S. \quad (7)$$

where

$$H(s) = \begin{bmatrix} G_{p\theta 1}(s) & 0 & 0 & 0 & 0 & 0 \\ 0 & G_{p\theta 2}(s) & 0 & 0 & 0 & 0 \\ 0 & 0 & G_{p\theta 3}(s) & 0 & 0 & G_{Q\theta}(s) \\ 0 & 0 & 0 & G_{EQ1}(s) & 0 & 0 \\ 0 & 0 & 0 & 0 & G_{EQ2}(s) & 0 \\ 0 & 0 & G_{PI3}(s) & 0 & 0 & 0 \end{bmatrix}.$$

3.2 Modeling of the feedback channel

Next, let's establish the model of the AC network, i.e., the feedback channel of the MIMO system.

As seen from Figure 5, the feedback channel reflects the power flow of the AC network. Since the input signals of the AC network contains the phase and magnitude of both the internal voltage and internal current, we need to derive the Jacobian matrix of the mixed system.

First, we calculate the branch circuit across each device. For the system shown in Figure 1, the current of each branch can be

TABLE 1 Results of modal analysis and robust stability margin in DVC timescale.

| $b_{H,L}$ | Dominant poles | Modified control parameters |
|-----------|--------------------|---|
| 0.7882 | $-3.97 \pm j5.85$ | $k_{p1a} = 8; k_{ppllr} = 50$ |
| 0.8413 | $-4.08 \pm j31.40$ | $k_{p1a} = 8.5; k_{ppllr} = 20; k_{lplr} = 150$ |
| 0.8037 | $-4.00 \pm j43.37$ | $k_{p2a} = 0.4; k_{ppllr} = 20; k_{lplr} = 150$ |
| 0.5965 | $-0.99 \pm j6.97$ | $k_{ppllr} = 2; k_{p1a} = 50$ |
| 0.4138 | $-0.98 \pm j31.60$ | $k_{ppllr} = 20; k_{p1a} = 2.3$ |

expressed as

$$\begin{aligned} \dot{I}_1 &= \frac{\dot{E}_1 - \dot{U}_t}{jX_1}, \\ \dot{I}_2 &= \frac{\dot{E}_2 - \dot{U}_t}{jX_2}, \\ \dot{I}_3 &= \dot{I}_3, \\ \dot{I}_g &= \frac{\dot{U}_g - \dot{U}_t}{jX_g}. \end{aligned} \tag{8}$$

According to the Kirchhoff's Current Law, the current flowing through the rectifier is

$$\dot{I}_1 + \dot{I}_2 + \dot{I}_g = \dot{I}_3. \tag{9}$$

Based on (8) and (9), the AC voltage on the bus can be calculated as

$$\dot{U}_t = \frac{-jX_1X_2X_g\dot{I}_3 + E_1X_2X_g + E_2X_1X_g + \dot{U}_gX_1X_2}{X_2X_g + X_1X_g + X_1X_2}. \tag{10}$$

By substituting (10) into (8), the current of the two GSCs can be obtained as

$$\begin{aligned} \dot{I}_1 &= Y_{11}\dot{E}_1 + Y_{12}\dot{E}_2 + G_{13}\dot{I}_3 + Y_{1g}\dot{U}_g, \\ \dot{I}_2 &= Y_{21}\dot{E}_1 + Y_{22}\dot{E}_2 + G_{23}\dot{I}_3 + Y_{2g}\dot{U}_g, \end{aligned} \tag{11}$$

where $Y_{11}, Y_{12}, G_{13}, Y_{1g}, Y_{21}, Y_{22}, G_{23}, Y_{2g}$ are the elements of the admittance matrix as shown in [Supplementary Appendix SA](#). The internal voltage of the rectifier can be described as

$$\dot{E}_3 = \dot{U}_t - j\dot{I}_3X_3. \tag{12}$$

By substituting (10) into (12), we have

$$\dot{E}_3 = Y_{31}\dot{E}_1 + Y_{32}\dot{E}_2 + G_{33}\dot{I}_3 + Y_{3g}\dot{U}_g, \tag{13}$$

where the elements of the admittance matrix $Y_{31}, Y_{32}, G_{33}, Y_{3g}$ are as shown in [Supplementary Appendix SA](#).

Then, the apparent power of the GSCs and the rectifier can be calculated as.

$$S_1 = E_1\dot{I}_1 = P_{out1} + jQ_1, \tag{14}$$

$$S_2 = E_2\dot{I}_2 = P_{out2} + jQ_2, \tag{15}$$

$$S_3 = E_3\dot{I}_3 = P_{out3} + jQ_3, \tag{16}$$

where $\overline{I_1}, \overline{I_2}, \overline{I_3}$ are conjugate of I_1, I_2, I_3 .

According to (11) and (13) into (14), the active power and reactive power of each branch can be expressed as.

$$\begin{aligned} P_{out1} &= G_{13}E_1I_3 \cos(\theta_1 - \theta_3) - jY_{12}E_1E_2 \sin(\theta_1 - \theta_2) \\ &\quad - jY_{1g}E_1U_g \sin\theta_1, \end{aligned} \tag{17}$$

$$\begin{aligned} Q_1 &= jY_{11}E_1^2 + G_{13}E_1I_3 \sin(\theta_1 - \theta_3) + jY_{12}E_1E_2 \\ &\quad \times \cos(\theta_1 - \theta_2) + jY_{1g}E_1U_g \cos\theta_1, \end{aligned} \tag{18}$$

$$\begin{aligned} P_{out2} &= G_{23}E_2I_3 \cos(\theta_2 - \theta_3) - jY_{21}E_1E_2 \sin(\theta_2 - \theta_1) \\ &\quad - jY_{2g}E_2U_g \sin\theta_2, \end{aligned} \tag{19}$$

$$\begin{aligned} Q_2 &= jY_{22}E_2^2 + G_{23}E_2I_3 \sin(\theta_2 - \theta_3) + jY_{21}E_1E_2 \\ &\quad \times \cos(\theta_2 - \theta_1) + jY_{2g}E_2U_g \cos\theta_2, \end{aligned} \tag{20}$$

$$\begin{aligned} P_{out3} &= Y_{31}E_1I_3 \cos(\theta_1 - \theta_3) + Y_{32}E_2I_3 \times \cos(\theta_2 - \theta_3) \\ &\quad + Y_{3g}I_3U_g \cos\theta_3, \end{aligned} \tag{21}$$

$$\begin{aligned} Q_3 &= Y_{31}E_1I_3 \sin(\theta_1 - \theta_3) + Y_{32}E_2I_3 \sin(\theta_2 - \theta_3) \\ &\quad - Y_{3g}U_gI_3 \sin\theta_3 - jG_{33}I_3^2. \end{aligned} \tag{22}$$

Linearizing (17) at the steady-state operating point yields.

$$\begin{aligned} \Delta P_{out1} &= K_{P\theta11}\Delta\theta_1 + K_{P\theta12}\Delta\theta_2 + K_{P\theta13}\Delta\theta_3 \\ &\quad + K_{PE11}\Delta E_1 + K_{PE12}\Delta E_2 + K_{PI13}\Delta I_3, \end{aligned} \tag{23}$$

$$\begin{aligned} \Delta Q_1 &= K_{Q\theta11}\Delta\theta_1 + K_{Q\theta12}\Delta\theta_2 + K_{Q\theta13}\Delta\theta_3 + K_{QE11}\Delta E_1 \\ &\quad + K_{QE12}\Delta E_2 + K_{QI13}\Delta I_3, \end{aligned} \tag{24}$$

$$\begin{aligned} \Delta P_{out2} &= K_{P\theta21}\Delta\theta_1 + K_{P\theta22}\Delta\theta_2 + K_{P\theta23}\Delta\theta_3 \\ &\quad + K_{PE21}\Delta E_1 + K_{PE22}\Delta E_2 + K_{PI23}\Delta I_3, \end{aligned} \tag{25}$$

$$\begin{aligned} \Delta Q_2 &= K_{Q\theta21}\Delta\theta_1 + K_{Q\theta22}\Delta\theta_2 + K_{Q\theta23}\Delta\theta_3 \\ &\quad + K_{QE21}\Delta E_1 + K_{QE22}\Delta E_2 + K_{QI23}\Delta I_3, \end{aligned} \tag{26}$$

$$\begin{aligned} \Delta P_{out3} &= K_{P\theta31}\Delta\theta_1 + K_{P\theta32}\Delta\theta_2 + K_{P\theta33}\Delta\theta_3 \\ &\quad + K_{PE31}\Delta E_1 + K_{PE32}\Delta E_2 + K_{PI33}\Delta I_3, \end{aligned} \tag{27}$$

$$\begin{aligned} \Delta Q_3 &= K_{Q\theta31}\Delta\theta_1 + K_{Q\theta32}\Delta\theta_2 + K_{Q\theta33}\Delta\theta_3 \\ &\quad + K_{QE31}\Delta E_1 + K_{QE32}\Delta E_2 + K_{QI33}\Delta I_3. \end{aligned} \tag{28}$$

In (23), $K_{P\theta11} \sim K_{P\theta33}, K_{PE11} \sim K_{PI33}, K_{Q\theta11} \sim K_{Q\theta33}, K_{QE33} \sim K_{QI33}$ are shown in [Supplementary Appendix SA](#). Denote

$$\begin{aligned} \mathbf{K}_{P\theta}(s) &= \begin{bmatrix} -K_{P\theta11} & -K_{P\theta12} & -K_{P\theta13} \\ -K_{P\theta21} & -K_{P\theta22} & -K_{P\theta23} \\ K_{P\theta31} & K_{P\theta32} & K_{P\theta33} \end{bmatrix}, \mathbf{K}_{PE}(s) = \begin{bmatrix} -K_{PE11} & -K_{PE12} & -K_{PE13} \\ -K_{PE21} & -K_{PE22} & -K_{PE23} \\ K_{PE31} & K_{PE32} & K_{PE33} \end{bmatrix}, \\ \mathbf{K}_{Q\theta}(s) &= \begin{bmatrix} K_{Q\theta11} & K_{Q\theta12} & K_{Q\theta13} \\ K_{Q\theta21} & K_{Q\theta22} & K_{Q\theta23} \\ K_{Q\theta31} & K_{Q\theta32} & K_{Q\theta33} \end{bmatrix}, \mathbf{K}_{QE}(s) = \begin{bmatrix} K_{QE11} & K_{QE12} & K_{QE13} \\ K_{QE21} & K_{QE22} & K_{QE23} \\ K_{QE31} & K_{QE32} & K_{QE33} \end{bmatrix}. \end{aligned} \tag{29}$$

TABLE 2 Results of modal analysis in DC voltage control timescale.

| | $k_{I_{pllr}}= 50; k_{Pr}= 1, k_{Ir}= 60;$ | |
|-------------------|--|----------------------------------|
| | $k_{i1a}= 1000; k_{p2a}= 2, k_{j2a}= 100;$ | |
| | $k_{p1b}= 50, k_{i1b}= 1000; k_{p2b}= 2, k_{j2b}= 100; k_{p7}= 0.05, k_{i7}= 20$ | |
| | $k_{P_{pllr}}= 2; k_{p1a}= 50$ | $k_{P_{pllr}}= 20; k_{p1a}= 2.3$ |
| $\lambda_{1,2}$ | -0.99 ±j6.97 | -0.98 ±j31.60 |
| $\lambda_{3,4}$ | -18.76 ±j40.62 | -10.15 ±j7.36 |
| $\lambda_{5,6}$ | -19.27 ±j39.44 | -19.30 ±j39.48 |
| $\lambda_{7,8}$ | -21.10 ±j31.48 | -20.07 ±j39.42 |
| $\lambda_{9,10}$ | -24.73 ±j19.65 | -22.37 ±j29.76 |
| $\lambda_{11,12}$ | -25.00 ±j19.37 | -24.81 ±j19.55 |
| λ_{13} | -26.17 | -26.22 |
| λ_{14} | -26.22 | -26.48 |
| λ_{15} | -808.96 | -808.77 |

Then, the feedback channel (23) can be written as

$$\Delta S = L(s) \Delta V. \tag{30}$$

where $L(s) = \begin{bmatrix} K_{P\theta}(s) & K_{PE}(s) \\ K_{Q\theta}(s) & K_{QE}(s) \end{bmatrix}$.

Then, the entire model of the system represented by transfer function matrix can be illustrated by Figure 6. In this model, ΔS represent the set of the input signals and ΔV represent the set of the output signals. $H(s)$ and $L(s)$ represent the forward and feedback channels, respectively.

4 Relative stability analysis and stable region computation

To analysis the relative stability of the system, we calculate the robust stability margin of the system first. Then, the methodology of assessing the stable region of parameters is illustrated.

4.1 Robust stability margin

In this subsection, we propose a new index, i.e., the robust stability margin based on the ν -gap metric to evaluate the relative stability of the MIMO system.

For a standard feedback system as depicted in Figure 6A, if the system is stable, the robust stability margin $b_{H,L}$ of Figure 6A are

defined as

$$b_{H,L} = \max_{\omega \in R \cup \infty} \bar{\sigma} \left(\left\| \begin{bmatrix} H(j\omega) \\ I \end{bmatrix} (I - L(j\omega)H(j\omega))^{-1} [-L(j\omega) \quad I] \right\| \right)^{-1}. \tag{31}$$

where $\bar{\sigma}$ refers to the maximum singular value. For a MIMO system represented by the transfer function matrix $G(s)$, the maximum singular value equals to the maximum eigenvalue of the product of the transfer function matrix $G(j\omega)$ and its conjugate transpose $G^*(j\omega)$. In addition, H_∞ norm denotes the maximum singular value of a system represented by transfer function matrix. Therefore, for the MIMO system with $H(s)$ as the forward channel and $L(s)$ as the feedback channel as shown in Figure 6A, if the system is stable, the robust stability margin can be expressed as

$$b_{H,L} = \left(\left\| \begin{bmatrix} H(s) \\ I \end{bmatrix} (I - L(s)H(s))^{-1} [-L(s) \quad I] \right\|_\infty \right)^{-1}. \tag{32}$$

The proposed robust stability margin can be used to assess the relative stability of the system. If the system is stable, $b_{H,L}$ is in the interval (0,1]. The larger $b_{H,L}$ is, the more stable the system is. When the system is unstable, $b_{H,L}$ equals to 0. Compared with other stability margin, i.e., phase margin and amplitude margin, the proposed robust stability margin can be directly computed in a MIMO systems.

4.2 Stable region of parameters

In this subsection, we will clarify the methodology of calculating the stable region of parameters. From the point view of control, the

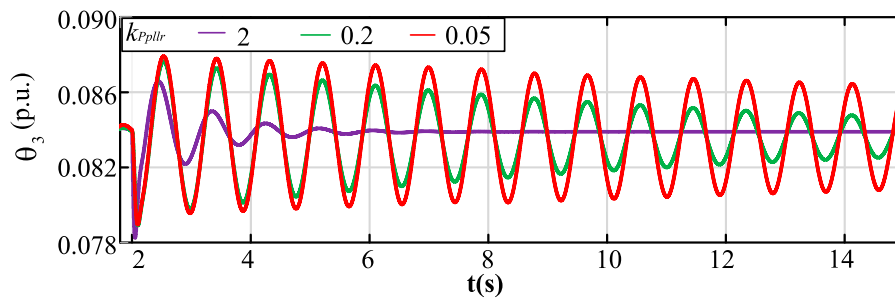


FIGURE 8 Time domain responses of θ_3 of the rectifier with different k_{pll_r} .

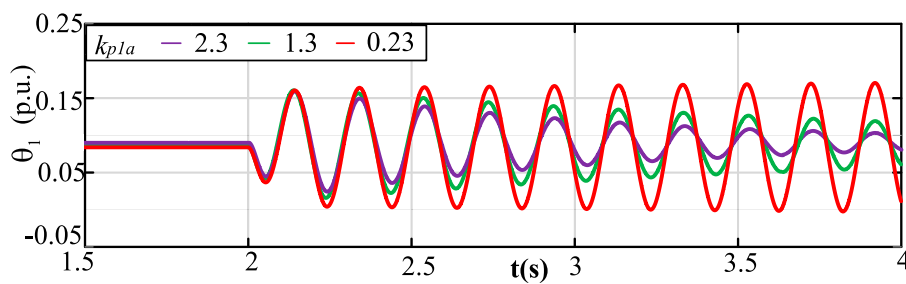


FIGURE 9 Time domain responses of θ_1 of GSC 1 with different k_{p1a} .

TABLE 3 Variation of $\arcsin r_{H,L}$ under different parameters of k_{p1a} .

| k_{p1a} | $\arcsin r_{H,L}$ |
|-----------|-------------------|
| 8 | 0 |
| 0.6 | 0.1791 |
| 0.1 | 0.2118 |

stable region for the control systems can be obtained by calculating the ranges of uncertain parameters preserving the system stability. In this paper, we mainly focus on assessing the stable region of the control parameters in DVC, DCC and PLL of the GSCs and the rectifier. The structure and the power flow of the network are considered to be fixed. It means that the uncertainties exist only in $\mathbf{H}(s)$.

Consider the feedback system with uncertainties as shown in Figure 6B. Denote $\tilde{\mathbf{H}}(s)$ as the set of uncertainties around the given system $\mathbf{H}(s)$. Denote the distance between $\mathbf{H}(s)$ and $\tilde{\mathbf{H}}(s)$ as $v[\mathbf{H}(s), \tilde{\mathbf{H}}(s)]$. According to the theory of v -gap (Zhou, 2010), the v -gap between the uncertain system in Figure 6B and the nominal system in Figure 6A can be calculated as

$$v[\mathbf{H}(s), \tilde{\mathbf{H}}(s)] = \left(1 - \left\| \begin{bmatrix} \mathbf{H}(s) \\ \mathbf{I} \end{bmatrix} \left(\mathbf{I} + \mathbf{H}(-s)^T \mathbf{H}(s) \right)^{-1} \left[\mathbf{H}(-s)^T \quad \mathbf{I} \right] \right\|_{\infty}^{-2} \right)^{\frac{1}{2}}. \tag{33}$$

Now, we present the stability criterion of the MIMO system with uncertainties in Figure 6B. Suppose the nominal MIMO system in Figure 6A is stable with the stability margin $v[\mathbf{H}(s), \tilde{\mathbf{H}}(s)]$. The uncertain system in Figure 3B is stable if and only if

$$\arcsin v[\mathbf{H}(s), \tilde{\mathbf{H}}(s)] < b_{H,L}. \tag{34}$$

Otherwise, the uncertain system is unstable.

We can use the proposed stability criterion in (34) to assess the stable region of parameters. Figure 7 shows the algorithm for calculating the stable region of parameters. Specifically, the flowchart is divided into three steps as follows.

Step 1 Check the stability of the system. If the system is unstable, set $b_{H,L} = 0$. Otherwise, compute $b_{H,L}$ of the nominal MIMO system in Figure 6A and continue.

Step 2 Assume the parameter $k = k_0$ in the nominal $\mathbf{H}(s)$ and the corresponding uncertain parameter $k = k_1$. Calculate the v -gap distance $v[\mathbf{H}(s), \tilde{\mathbf{H}}(s)]$.

Step 3 If $\arcsin v[\mathbf{H}(s), \tilde{\mathbf{H}}(s)] < b_{H,L}$, the uncertain system with $k = k_1$ is stable. Otherwise, the system with $k = k_1$ is unstable.

Step 4 Using the incremental search, find the smallest k_1 and the largest k_1 so that the system is stable. Then the stable region for parameter k is $(k_{1,smallest}, k_{1,largest})$.

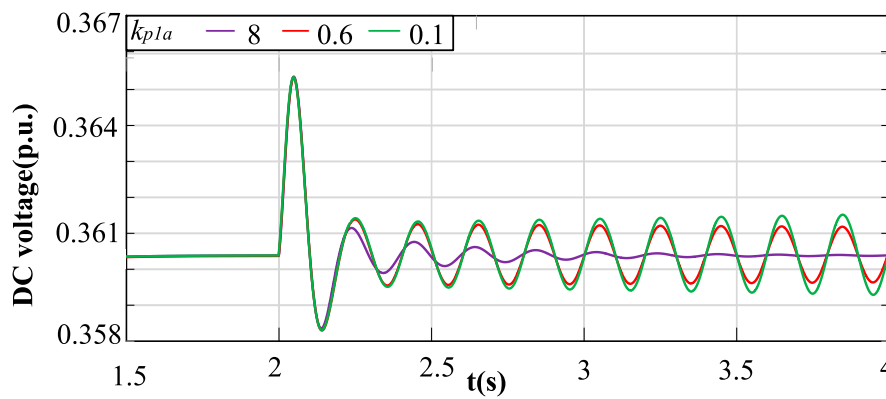


FIGURE 10 Nonlinear time-domain simulation.

TABLE 4 Variation of SCR and $\arcsin r_{H,L}$ under different parameters of X_g .

| X_g | SCR | $\arcsin r_{H,L}$ |
|-------|------|-------------------|
| 0.35 | 4.29 | 0 |
| 0.43 | 3.49 | 0.1846 |
| 0.44 | 3.41 | 0.1972 |

5 Simulation results

This section presents the simulation results to demonstrate the superiority of this method. We first calculate the robust stability margin of the MIMO system and compare with the results of eigenvalue analysis. Then, we present how to calculate the stable region of the parameters of PLL and X_g utilizing the method.

5.1 Relative stability evaluation

Recall the HVDC system connected with GSCs as shown in Figure 1. Common operation points and control parameters are provided in Supplementary Appendix SA. With five different sets of control parameters, we calculate the robust stability margin of the systems. The results are shown in Table 1. We can see that the second system has the largest robust stability margin, which means it has the best stability performance. The fifth system has the smallest robust stability margin, which indicates the worst stability performance.

Next, we compare the results with eigenvalue analysis. Table 2 shows the results of the eigenvalues and participation factors with two given sets of parameters. We can see that both of the two systems are stable since the eigenvalues are all in the left half plane. In addition, the real parts of the dominant poles of the two systems are close to each other. It seems that the relative stability of the systems are close. However, the relative stability of the systems are different according to the robust stability margin calculated by our proposed method. It can be verified by time-domain simulation

based on detailed nonlinear model. According to the participation factors, k_{ppll_r} and k_{p1a} have the greatest influence on the dominant poles of the two systems, respectively. Figure 8 shows the time domain response of θ_3 of the rectifier with different k_{ppll_r} . When k_{ppll_r} changes from 2 to 0.05, the system remains stable. Figure 9 shows the time domain responses of θ_1 of GSC 1 with different k_{p1a} . When k_{p1a} changes from 2.3 to 0.23, the system changes from stable to unstable. The results show that the system with $k_{ppll_r} = 2$ and $k_{p1a} = 50$ can tolerate a larger range of parameter variation than the system with $k_{ppll_r} = 20$ and $k_{p1a} = 2.3$, which means the former is more robust.

5.2 Stable region of the parameters

In this subsection, we show how to calculate the stable region of the parameters of k_{p1a} and X_g in the MIMO system.

First, we focus on the proportional parameter k_{p1a} of PLL control in GSC 1. Consider the MIMO system with parameters given in Supplementary Appendix SA. According to the expressions of robust stability margin (32), the robust stability margin of the system is 0.19. Based on the algorithm proposed in Section 2.3.2, when k_{p1a} varies, we can compute the v -gap $v[\mathbf{H}(s), \tilde{\mathbf{H}}(s)]$ between $\mathbf{H}(s)$ and $\tilde{\mathbf{H}}(s)$. The results are shown in Table 3. It can be seen that $v[\mathbf{H}(s), \tilde{\mathbf{H}}(s)]$ gradually increases when k_{p1a} decreases. $v[\mathbf{H}(s), \tilde{\mathbf{H}}(s)]$ equals to 0.1791, which is close to 0.19 when $k_{p1a} = 0.6$. $v[\mathbf{H}(s), \tilde{\mathbf{H}}(s)]$ is slightly over the stability margin 0.19 when $k_{p1a} = 0.1$. Time-domain simulation based on the nonlinear model in Figure 10 verifies the results. The system is in a critically stable state when $k_{p1a} = 0.6$. The system oscillates when $k_{p1a} = 0.1$. Therefore, to maintain the stability of the system, the value of the proportional parameter k_{p1a} of PLL control of GSC 1 should be greater than 0.6.

Then, we compute the stable region of the reactance between the infinite bus and the point of interconnection X_g . As we know, X_g affects the short-circuit ratio (SCR) of the system. With the parameters shown in Supplementary Appendix SA (where $X_g = 0.35$), the robust stability margin of the system is 0.19. Table 4 shows the v -gap $v[\mathbf{H}(s), \tilde{\mathbf{H}}(s)]$ between $\mathbf{H}(s)$ and $\tilde{\mathbf{H}}(s)$ when X_g changes. We can see that $v[\mathbf{H}(s), \tilde{\mathbf{H}}(s)]$ increases when X_g increases.

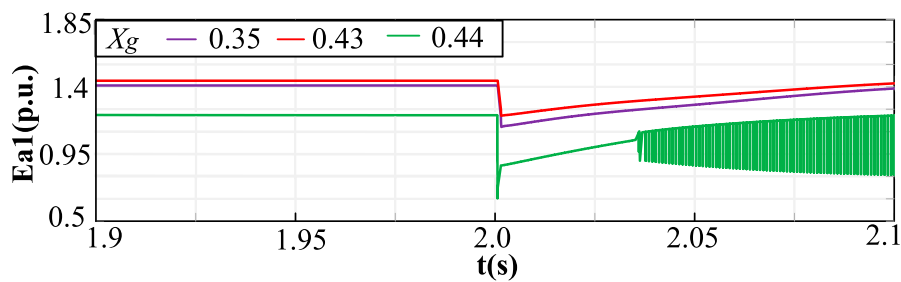


FIGURE 11
Nonlinear time-domain simulation.

$\nu[\mathbf{H}(s), \tilde{\mathbf{H}}(s)]$ equals to 0.1846, which is close to 0.19 when $X_g = 0.43$. It indicates that the system is critically stable with the corresponding $SCR = 3.49$. Then, when $X_g = 0.44$, $\nu[\mathbf{H}(s), \tilde{\mathbf{H}}(s)]$ is larger than 0.19, which means that the system is unstable. Time domain simulation shown in Figure 11 based on the nonlinear model verifies the results.

The above two cases show the effectiveness of the proposed method to compute the stable regions of parameters. It is worth noticing that the results do not have conservatism since the stability criterion is a necessary and sufficient condition.

6 Conclusion

This paper analyzes the relative stability of a HVDC system connected with WFs utilizing the ν -gap metric. We build a MIMO system model of such a system represented by transfer function matrix. Then, a new stability index, which is called the robust stability margin, is proposed to assess the relative stability of a HVDC system connected with WFs. It can indicate how far the system is from instability. The larger the robust stability margin, the more stable the system performs. Next, a method to compute the stable region of control parameters is presented based on the sufficient and necessary stability criterion of the ν -gap metric. Simulations demonstrate the effectiveness of the proposed method. In future research, we would utilize this method to other MIMO systems containing renewable energies, for instance, to analyze the stability of a system with multiple wind turbines. Moreover, we will further explore parameter design methods for other MIMO systems to reach the maximize stability margin of the system.

Data availability statement

The original contributions presented in the study are included in the article/Supplementary Material, further inquiries can be directed to the corresponding author.

Author contributions

KJ: Data curation, Writing–review and editing. CY: Supervision, Writing–review and editing. WZ: Methodology, Supervision,

Writing–original draft, Writing–review and editing. YC: Validation, Writing–original draft, Writing–review and editing. PX: Investigation, Methodology, Writing–review and editing. LL: Investigation, Methodology, Supervision, Writing–review and editing. PH: Investigation, Methodology, Supervision, Writing–review and editing.

Funding

The author(s) declare financial support was received for the research, authorship, and/or publication of this article. This work was partially supported by the science and technology project of State Grid Corporation of China, project number: 4000-20222070A-1-1-ZN, and partially by the National Natural Science Foundation of China under Grant 62303356.

Conflict of interest

The authors declare that the research was conducted in the absence of any commercial or financial relationships that could be construed as a potential conflict of interest.

The authors declare that this study received funding from State Grid Corporation of China. The funder had the following involvement: Data analysis and writing of the article.

Publisher's note

All claims expressed in this article are solely those of the authors and do not necessarily represent those of their affiliated organizations, or those of the publisher, the editors and the reviewers. Any product that may be evaluated in this article, or claim that may be made by its manufacturer, is not guaranteed or endorsed by the publisher.

Supplementary material

The Supplementary Material for this article can be found online at: <https://www.frontiersin.org/articles/10.3389/fenrg.2024.1379009/full#supplementary-material>

References

- Ángel Cardiel-Álvarez, M., Rodríguez-Amenedo, J. L., Arnaltes, S., and Montilla-Djesus, M. E. (2017). Modeling and control of lcc rectifiers for offshore wind farms connected by hvdc links. *IEEE Trans. Energy Convers.* 32, 1284–1296. doi:10.1109/TEC.2017.2696261
- Bayhan, N., and Soylemez, M. T. (2007). “A new technique for calculation of maximum achievable gain and phase margins with proportional control,” in 2007 Mediterranean Conference on Control & Automation, China, 27–29 June 2007 (IEEE), 1–6.
- Jiang, Y., Yu, W., Yu, W., and Wen, C. (2021). “On gradation and classification of faults for permanent magnet synchronous motor systems based on v-gap metric,” China, 2021 IEEE 10th Data Driven Control and Learning Systems Conference (DDCLS) (IEEE).
- Kovacevic, S., Jovcic, D., Despouys, O., and Rault, P. (2019). “Eigenvalue study of torsional interactions between gravelines generator and ifa2000 hvdc,” in 2019 20th International Symposium on Power Electronics (Ee), USA, 23–26 Oct. 2019 (IEEE), 1–6.
- Liu, H., Shah, S., and Sun, J. (2014). “An impedance-based approach to hvdc system stability analysis and control development,” in 2014 International Power Electronics Conference (IPEC-Hiroshima 2014 ECCE-ASIA) (IEEE), China, 18–21 May 2014 (IEEE).
- Liu, H., and Sun, J. (2013a). “Modeling and analysis of dc-link harmonic instability in lcc hvdc systems,” in 2013 IEEE 14th Workshop on Control and Modeling for Power Electronics (COMPEL) (IEEE), USA, 23–26 June 2013 (IEEE).
- Liu, H., and Sun, J. (2013b). “Small-signal stability analysis of offshore wind farms with lcc hvdc,” in 2013 IEEE Grenoble Conference, China, 16–20 June 2013 (IEEE), 1–8.
- Lu, J., Yuan, X., Hu, J., Zhang, M., and Yuan, H. (2020). Motion equation modeling of lcc-hvdc stations for analyzing dc and ac network interactions. *IEEE Trans. Power Deliv.* 35, 1563–1574. doi:10.1109/TPWRD.2019.2947572
- Rohit, C., Darji, P. B., and Jariwala, H. (2021). “A stability assessment and estimation of equivalent damping gain for ssr stability by nyquist stability criterion in dfig-based windfarms,” in 2021 31st Australasian Universities Power Engineering Conference (AUPEC), USA, 26–30 Sept. 2021 (IEEE), 1–6.
- Shen, J., Liu, C., Su, C., Li, H., and Wei, W. (2021). “Deepening research on state space analytical model of hvdc transmission system,” in 2021 IEEE 4th International Electrical and Energy Conference (CIEEC), China, 28–30 May 2021 (IEEE), 1–4.
- Su, Y., Cao, R., Xin, Q., Xie, H., Liu, H., and Huang, W. (2023). “Equivalent impedance modeling of lcc-hvdc control system based on transfer function method,” in 2023 6th International Conference on Energy, Electrical and Power Engineering (CEEPE), USA, 12–14 May 2023 (IEEE), 813–818.
- Sun, J. (2011). Impedance-based stability criterion for grid-connected inverters. *IEEE Trans. Power Electron.* 26, 3075–3078. doi:10.1109/TPEL.2011.2136439
- Vinnicombe, G. (2001). Uncertainty and feedback. h ∞ loop-shaping and the v-gap metric. *IEEE*. doi:10.1142/9781848160453
- Wang, M., Chen, Y., Dong, X., Hu, S., Liu, B., Yu, S. S., et al. (2022a). Impedance modeling and stability analysis of dfig wind farm with lcc-hvdc transmission. *IEEE J. Emerg. Sel. Top. Circuits Syst.* 12, 7–19. doi:10.1109/JETCAS.2022.3144999
- Wang, M., Li, Z., Dong, X., Liu, B., Su, W., and Zhang, X. (2020). “Sequence impedance modeling of dfig wind farm via lcc-hvdc transmission,” in 2020 Chinese automation congress (CAC) (IEEE) (New York: IEEE), 5320–5325.
- Wang, X., Shi, P., Liu, Y., Nian, H., Chen, Z., and Chen, G. (2022b). “Impedance-based stability analysis of lcc-hvdc connected to weak grid considering frequency coupling characteristic,” in 2022 IEEE 5th International Electrical and Energy Conference (CIEEC) (IEEE), China, May 27 – 29, 2022 (IEEE), 153–157.
- Yogarathinam, A., Kaur, J., and Chaudhuri, N. R. (2017). “Impact of inertia and effective short circuit ratio on control of frequency in weak grids interfacing lcc-hvdc and dfig-based wind farms,” in *IEEE transactions on power delivery* (Germany: IEEE), 2040–2051.
- Yuan, H., Yuan, X., and Hu, J. (2017). Modeling of grid-connected VSCs for power system small-signal stability analysis in DC-link voltage control timescale. *IEEE Trans. Power Syst.* 32, 3981–3991. doi:10.1109/tpwrs.2017.2653939
- Zhou, H., Yang, G., and Wang, J. (2011). Modeling, analysis, and control for the rectifier of hybrid hvdc systems for dfig-based wind farms. *IEEE Trans. Energy Convers.* 26, 340–353. doi:10.1109/TEC.2010.2096819
- Zhou, K. (2010). *Introduction to feedback control* (introduction to feedback control).